minerals

MDPI

Article

Steel Slag Characterisation—Benefit of Coupling Chemical, Mineralogical and Magnetic Techniques

Maud Herbelin [1,*], Jérôme Bascou [1], Véronique Lavastre [1], Damien Guillaume [1], Mhammed Benbakkar [2], Steve Peuble [3] and Jean-Philippe Baron [4]

[1] Université de Lyon, UJM–Saint–Etienne, CNRS, Laboratoire Magmas et Volcans UMR 6524, F-42023 Saint-Etienne, France; jerome.bascou@univ-st-etienne.fr (J.B.); veronique.lavastre@univ-st-etienne.fr (V.L.); damien.guillaume@univ-st-etienne.fr (D.G.)

[2] Université Clermont Auvergne, CNRS, IRD, OPGC, Laboratoire Magmas et Volcans, F-63000 Clermont-Ferrand, France; m.benbakkar@opgc.univ-bpclermont.fr

[3] Mines Saint-Étienne, Centre "Sciences des Processus Industriels et Naturels" (SPIN), Département "Procédés pour l'Environnement et les Géo-ressources" (PEG), UMR 5600 EVS, UMR 5307 LGF, F-42023 Saint-Étienne, France; steve.peuble@emse.fr

[4] INDUSTEEL FRANCE Groupe ArcelorMittal, B.P. 368, 42803 Rive de Gier, France; jean-philippe.baron@arcelormittal.com

* Correspondence: maud.herbelin@univ-st-etienne.fr

Received: 16 June 2020; Accepted: 3 August 2020; Published: 9 August 2020

Abstract: Steel-making slag is largely used today in road construction and other applications, but significant volumes are landfilled and cannot be recycled for excessive contents in hazardous metals, such as chromium or vanadium. The long-term behaviour of this material is still little known, and the characterisation of large volume slag dumps remains an environmental challenge. In this study various analytical techniques are used to characterise Electric Arc Furnace (EAF) slag landfilled for several decades and exposed to chemical weathering and erosion. Coupling chemical, mineralogical and magnetic techniques helps to understand the relations between hazardous metals and mineral phases. A special interest is given to Fe-bearing minerals microstructure so as to link the magnetic properties of the material to its mineralogical composition. The studied slag presents high amounts of chromium (between 1 and 3 wt. %) and very high magnetic susceptibility values (near 60×10^{-6} m^3/kg), explained by the presence of magnetite and a spinel solid solution. Some correlations are found between magnetic susceptibility and potentially hazardous metals, providing new perspectives for future environmental investigations.

Keywords: Electric Arc Furnace Slag; landfilling; mineralogy; hazardous metals; chromium; magnetic susceptibility

1. Introduction

More than 400 million tonnes of iron and steel slag are produced each year in the world [1,2]. In Europe, about 18 million tonnes of steel slag were produced each year from 2000 to 2016 [3]. An important part of this slag can be recycled as aggregates for road construction, as additives in cement and concrete production, as fertilizers and various others uses, but between 1 and 4 million tonnes per year are landfilled. This part remains unusable because of the presence of potentially hazardous metals. Electric Arc Furnace (EAF) slag, which present high contents in chromium (Cr), vanadium (V) and molybdenum (Mo), often fall into that category. They result from recycled steel scrap melting and represent between 30% and 40% of the total steel-making slag production. The European directive 1999/31/CE [4] about waste landfilling encourages the companies to change their process in order to produce heavy metal-free EAF slag for recycling. However, the significant volumes of former

slag accumulated before in open landfill sites need to be monitored, especially when they are exposed to meteoric weathering and are likely to release hazardous metals.

Anticipating the leaching behaviour of slag is a major issue today. An in-depth study of the chemical and mineralogical properties is necessary beforehand. They depend on the nature of the materials added during the process (steel scrap, lime, fluxes, alloying elements), the targeted steel grade, furnace conditions, and cooling rate. In EAF slag, the major chemical compounds are Ca, Si, Fe, Mg and Al and the most common mineralogical phases are silicates such as larnite (Ca_2SiO_4), bredigite ($Ca_7Mg(SiO_4)_4$), merwinite ($Ca_3MgSi_2O_8$) and mellilite ($Ca_2(Mg,Al,Fe)(Si,Al)_2O_7$), ferrites and aluminates such as brownmillerite ($Ca_2(Al,Fe)_2O_5$) and mayenite ($12CaO{\cdot}7Al_2O_3$), and metal oxides such as wustite ((Fe,Mg,Mn)O) and spinel ($(Mg,Mn)(Cr,Fe,Al)_2O_4$) [5–10]. Even when rapidly cooled, EAF slag tends to have very crystalline structure due to their high basicity [9,11–13]. However, cooling conditions do influence the nature and the size of some mineral phases. Crystal size tends to decrease for high cooling rate, particularly for spinel minerals [13,14]. Rapid cooling also promotes the formation of metastable phases and increases the reactivity with water [11,14].

Concerning potentially hazardous elements such as Cr and V, the first question that arises is about their location and their speciation, since both have a great influence on their mobility and bioavailability. Engström et al. [15], Mombelli et al. [7] and Neuhold et al. [8] report the presence of Cr(III) in spinel solid solutions ($(Mg,Mn)(Cr,Fe,Al)_2O_4$). Mombelli et al. [7] also mention the presence of Cr(III) in calcium chromite ($CaCr_2O_4$). V is mainly found as a trace in the spinel phases according to Neuhold et al. [8], while Mombelli et al. [7] also report the presence of V in brownmillerite ($Ca_2(Fe,Al,Cr)_2O_5$) and larnite (Ca_2SiO_4). These studies use X-ray diffraction (XRD) combined with scanning electron microscopy (SEM equipped with energy dispersive spectroscopy probe) or electron microprobe analyses (EMPA). Piatak et al. [1] outline that these techniques are not always sufficient to accurately characterise the mineralogy. One of the reasons is the presence of submicrometer-size inclusions or a mixture of phases on a nanometre-scale. Raman spectroscopy and transmission electron microscopy (TEM) are suggested as additional methods.

Another question is how to characterise very large volumes of material while the techniques mentioned above work at the micrometre scale. That is why magnetic measurements, which are quick to implement and easy to deploy at the field scale should be considered. Assuming that heavy metals can be spatially associated to Fe bearing phases, it appears interesting to study the magnetic properties of slag. Indeed, magnetic susceptibility has been widely used as a proxy for industrial pollution assessment in soils and sediments [16–20]. Gołuchowska et al., Jordanova et al., Magiera et al., and Szuszkiewicz et al. [21–24] studied the magnetic properties of various industrial wastes, such as lagooned ashes from blast furnace, fly ashes from power plants, cement dust and lime dust, but very few studies deal with the magnetic aspects of steel-making slag. Rosowiecka and Nawrocki [16] used magnetic measurements on soils to evaluate the pollution extent in the surroundings of ironworks but did not mention the presence of slag. Some other studies used magnetic methods on ancient iron production sites for archaeological purposes; for instance, to delineate ancient slag heaps [25,26].

The present study focuses on partially weathered EAF slag coming from the steel-making plant of Châteauneuf (Loire, France). A considerable volume (>200,000 m^3) was accumulated between 1950 and 2006 and landfilled because its excessive chromium content prevents any kind of recycling. This material is exposed to chemical weathering and erosion. The presence of habitations near the site and the proximity of a river associated with alluvial groundwater reinforce the concerns about environmental aspects. In this context, the mineralogical characterisation of the material is fundamental in order to predict its long-term behaviour regarding metal elements release. Various analytical techniques are used to better understand the chemical and mineralogical properties of this slag (energy-dispersive X-ray fluorescence, induced coupled plasma-atomic emission spectrometry, XRD, EMPA and Raman spectroscopy). In addition, the study gives a particular interest to magnetic methods—Magnetic susceptibility measurements and thermomagnetic curves are performed in laboratory. It allows to

complete the mineralogical information about magnetic phases in slag and to extend the already existing magnetic data on industrial wastes.

2. Materials and Methods

2.1. Sampling

The material studied comes from the Industeel France Arcelor Mittal site of Châteauneuf (Loire, France) where a very large volume of slag was accumulated over six decades and spread over a surface of approximately 4 ha, with a thickness varying between 2 and 9 m. The site is located in an urban area, surrounded by a highway and a railway. The slag lies on the alluvial deposits of the Gier River. This study focuses on the surface layer which, in contact with rainwater and the atmosphere, should reveal the most significant transformations. Thirty samples of approximately 300 g of EAF slag (named slag-1 to slag-30) were collected on the slag dump surface, up to 10 cm deep, along two 150 m profiles, with a sampling step of 10 m (Figure 1).

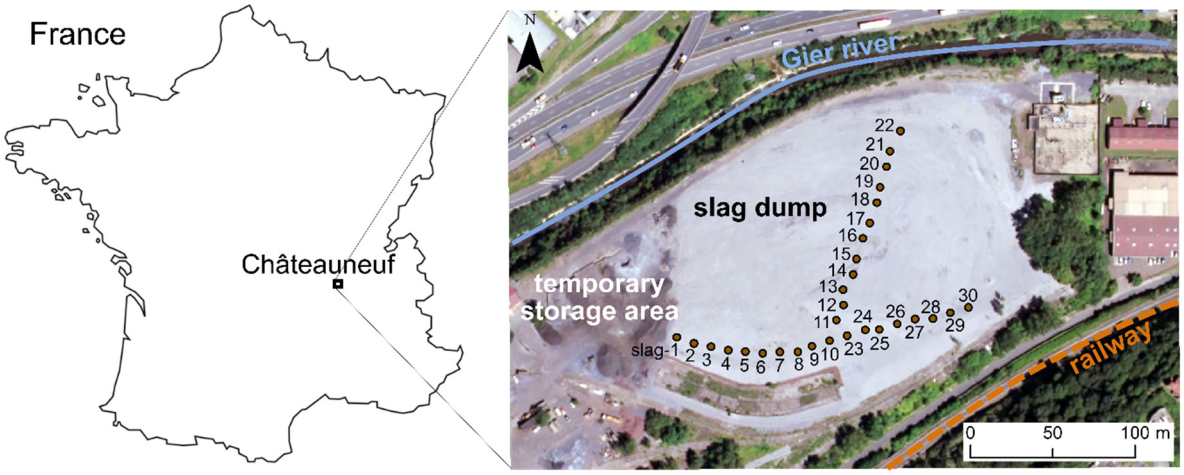

Figure 1. Aerial photograph of the studied site and sampling points.

All of the material collected was dried at 60 °C in an oven. Then different treatments (sub-sampling, grinding, sieving) were applied depending on the type of analysis.

- Two sub-samples of 8 cm^3 (approximately 15 g) were taken with a beaker from each of the 30 initial samples for magnetic and chemical analyses. This method allows to evaluate the variability within the same sample and provides a sufficient amount of data for a statistical analysis (see Section 2.2.4). These samples are hereafter referred to as "slag-1A", "slag-1B", "slag-2A", "slag-2B" and so forth.
- The sample slag-13, representative of the average chemical composition of the 30 EAF slag samples (Table 2), was selected to be sieved so as to explore the main properties of the slag as a function of grain size. Eight grain size fractions were examined: <0.25 mm, 0.25–0.5 mm, 0.5–1.0 mm, 1.0–1.6 mm, 1.6–2.5 mm, 2.5–5 mm, 5–10 mm and >10 mm.
- A last sample called Mix 1 was prepared by mixing equal volumes from each of the 30 initial samples (16 cm^3 taken with a beaker). It was then roughly crushed with a jaw crusher, to a size smaller than 4 mm, with the aim to get a representative set of grains the size of which is convenient for micro-analyses (EMPA and Raman spectroscopy) and thermo-magnetic measurements (0.5–1.0 mm).

In order to evaluate the potential for magnetic measurements to discriminate slag from other materials, rock samples were taken in the vicinity of the site. Surrounding rock formations consist of gneisses, micachists and coal sediments. One sample of gneiss, one sample of micaschist and one sample of coarse sandstone were collected from rocky outcrops within a 1-km radius of the site.

2.2. Laboratory Methods and Procedures

2.2.1. Bulk Chemical Analyses

Bulk chemical analyses were performed on the 60 sub-samples "slag1A", slag1B" and so forth, at Laboratoire Magmas et Volcans, Saint-Etienne, France, with an energy-dispersive X-ray fluorescence (ED-XRF) analyser (Olympus Vanta serie M). The samples were finely ground with a ring mill (median grain size ≈ 20 μm) and compacted in capsules.

The different particle size fractions from the sample slag-13 were solubilized by alkali fusion in order to perform bulk chemical analyses by ICP-AES (induced coupled plasma-atomic emission spectrometry). Each sample was finely ground and 100 mg of the powder was mixed with 300 mg of $LiBO_2$ in a porcelain dish. It was then transferred to a graphite crucible and fused for 5 min at about 1100 °C in an induction furnace (2 kW). The bead obtained was dissolved in an acidic solution of HNO_3 (1 M) and, after complete dissolution the solution was filtered to remove graphite particles. ICP-AES measurements were done at Laboratoire Magmas et Volcans, Clermont-Ferrand, France using ULTIMA C spectrometer (Horiba scientific, Jobin-Yvon), with an incident power of 1.1 kW and a reflected power <15 W. Reference materials GH (for Si, Na, K) and BR (for the other elements), both from Centre de Recherches Pétrographiques et Géochimiques (CRPG), Nancy, France, provided high points of the calibration lines, while a pure $LiBO_2$ solution (300 mg in 200 mL of 1M HNO_3) was used as the zero.

Double chemical analyses were performed on a subset of 17 slag samples by alkali fusion/ICP-AES and ED-XRF. The results showed good correlations between the two techniques and assessed the reliability of ED-XRF. This latter technique is much faster and was favoured when many samples had to be analysed.

In addition to chemical analyses, loss on ignition (LOI) was measured on the different particle size fractions of sample slag 13. Each sample was weighted before and after heating at 110 °C and 1000 °C. The mass lost at 110 °C gives information on the amount of adsorbed water, while the mass lost at 1000 °C shows the presence of hydroxides and carbonates [27]. In addition, total carbon contents were measured on the same samples at Laboratoire Magmas et Volcans in Saint-Etienne using an elemental analyser—Thermo Isolink.

2.2.2. Mineralogical Characterisation

X-ray diffraction (XRD) analyses were performed at Mines de Saint-Etienne by a Bruker D8 A25 diffractometer equipped with Cu radiation (WL = 1.5406 Å) on the eight particle size fractions. Each one was previously ground in the same conditions as for ED-XRF analyses (see Section 2.2.1).

Electron Microprobe and Raman analyses were done on 0.5–1 mm grains of slag. A total of 112 grains was selected from Mix 1 and moulded in epoxy resin. The five blocks obtained were lapped with a silicon carbide powder and ethanol and polished with diamond paste. The polished sections were then metallized with carbon for electron microprobe analyses (EMPA). Subsequently, the grains studied are designated by the number of the block to which they belong and by their number within the block, for example, grain 25, block 1.

Two types of EMPA analyses were performed—Point quantitative analyses and quantified chemical maps, both using the Cameca SxFiveTactis microprobe at Laboratoire Magmas et Volcans in Clermont-Ferrand.

For point quantitative analyses, the acceleration voltage was 15 kV and the current was 15 nA; the wavelength dispersive spectrometer mode was used for all the elements. Kα emissions were measured with the help of the following crystals—TAP (thallium acid phthalate) on spectrometer 1 for Si, Al, and Mg, LPET (pentaerythritol, line L) on spectrometer 2 for P and V, LLIF (lithium fluoride, line L) on spectrometer 3 for Fe, Mn and Cr and PET (pentaerythritol) on spectrometer 4 for Ca and Ti. The instrument was calibrated with the following standards—wollastonite for Ca and Si, $TiMnO_3$ for Ti and Mn, Fe_2O_3 for Fe, Al_2O_3 for Al, orthoclase for K, MgO for Mg, metallic Mo for Mo, apatite for

P, vanadinite for V and Cr_2O_3 for Cr. A more important number of analyses were performed for the minerals found to be particularly heterogeneous.

Quantified EMPA chemical maps were generated with an acceleration voltage of 15 kV and a current of 30 nA. The step size was 0.4 µm and the dwell time was 30 ms. Mg, Al and Mn were measured in energy dispersive spectroscopy (EDS) mode and Si, Cr, Fe and Ca in wavelength dispersive spectroscopy (WDS) mode, Si with TAP on spectrometer 1, Cr with LPET on spectrometer 2, Fe with LLIF on spectrometer 3 and Ca with PET on spectrometer 4. Under these conditions, the resolution of the images is finer than the spatial resolution of the chemical analyses. This means that in the case of very fine intergrowths (<1 µm), the analyse also takes into account adjacent phases. Raman spectroscopic measurements were performed at Mines Saint-Etienne (France) using a confocal XploRA Raman microscope (Horiba Jobin–Yvon) equipped with a laser operating at 532 nm. Analyses were acquired with a laser power of 10 mW after calibration of the spectrometer by Si line at 520 ± 1 cm^{-1}. The spatial and spectral resolutions of the measurements were 2 µm and 1 cm^{-1}, respectively. Raman spectra were carried out between 250 and 1750 cm^{-1}, depending on the samples, to characterise the internal and lattice modes of mineral phases. Data were collected for 30 to 40 s and averaged over three accumulation cycles.

2.2.3. Magnetic Measurements

Mass specific magnetic susceptibility was measured using an MFK1-FA susceptibility bridge (AGICO) at Laboratoire Magmas et Volcans in Saint Etienne, on the samples slag-1A, slag-1B, … slag-30B, under weak magnetic field (200 A/m) and low frequency (976 Hz). Magnetic susceptibility of surrounding rocks samples was also measured with the same equipment.

Thermomagnetic analyses of low field magnetic susceptibility κ(T) were performed on the MFK1-FA susceptibility bridge with CS-4 and CS-L attachments (AGICO) at Laboratoire Magmas et Volcans in Saint Etienne. Thermomagnetic curves were carried out on 0.5–0.8 mm grains from Mix-1. For high temperature measurements, the furnace CS-4 gradually heated the samples from 20 to 700 °C under inert atmosphere (argon gas). For low temperature measurements, the samples were cooled down to −192 °C with liquid nitrogen and then gradually heated to room temperature (approximately 20 °C) with the cryostat CS-L.

2.2.4. Principal Component Analysis

A Principal Component Analysis (PCA) was carried out on the set of samples slag-1A, slag-1B … slag-30B, using 10 variables—Magnetic susceptibility previously measured with MFK1-FA Kappabridge and FeO, CaO, Al_2O_3, SiO_2, MnO, Cr_2O_3, MgO, V_2O_3 and MoO_3 contents obtained with ED-XRF analyses. This approach aims to relate chemical components to magnetic susceptibility. The PCA was performed with R thanks to the libraries "FactoMineR" and "factoextra", and the function "PCA". It is carried out in two steps—Normalization of the data set, followed by Eigen values decomposition of the data covariance matrix.

3. Results

3.1. Bulk Chemical Composition

The average chemical composition of the 60 samples slag-1A to slag-30B is given in Table 1. Detailed results obtained for each sample are given in Supplementary Material, Table S1. Major elements are Ca, Fe and Si, with a CaO/SiO_2 mass ratio of 3.15. In addition, Table 2 shows the variation in bulk chemical composition as a function of grain size. Coarser fractions are richer in Fe, Si, Mn, P, Ti and V while finer fractions are richer in Mg and Al. They are also richer in volatile elements such as C, H and O according to total carbon analyses and LOI at 1000 °C. Mo could not be measured by ICP-AES.

Table 1. Bulk chemical composition (wt. %) of the 60 samples (slag-1A … slag-30B) obtained by Xray fluorescence (ED-XRF) analyses.

wt. %	Mean	Min	Max
MgO	4.29	2.58	5.53
Al_2O_3	5.65	4.49	10.10
SiO_2	9.70	7.90	21.00
P_2O_5	0.40	0.32	0.45
CaO	30.58	24.73	32.87
TiO_2	0.24	0.19	0.32
V_2O_3	0.03	0.02	0.04
Cr_2O_3	2.83	2.00	3.66
MnO	5.27	3.62	6.16
FeO *	29.86	21.64	34.49
MoO_3	0.05	0.05	0.07

* Total Fe expressed as FeO.

Table 2. Bulk chemical composition (wt. %) of the different particle size fractions of slag-13 (obtained by ICP-AES analyses, carbon contents measured by elemental analyser) and loss on ignition mass percentage (LOI) at 110 °C and 1000 °C. N.B.: bulk chemical composition obtained by ED-XRF analysis for the initial sample slag-13 (before sieving) is given as a reference.

	Initial Sample (ED-XRF)	**Slag-13—Chemical Composition of the Different Grain Size Fractions (ICP-AES—Elemental Analyser)**							
Grain Size (mm)	**Total**	**>10**	**5–10**	**2.5–5**	**1.6–2.5**	**1.0–1.6**	**0.5–1.0**	**0.25–0.5**	**<0.25**
Distribution	**(100%)**	**(20%)**	**(18%)**	**(32%)**	**(6%)**	**(11%)**	**(8%)**	**(3%)**	**(2%)**
(wt. %)									
MgO	3.59	5.14	4.53	5.23	5.46	5.50	5.48	5.87	7.36
Al_2O_3	4.73	4.43	4.43	4.42	4.80	4.88	5.37	6.66	6.93
SiO_2	8.25	9.15	7.89	7.76	7.63	7.25	7.78	7.62	6.61
P_2O_5	0.41	0.54	0.38	0.39	0.37	0.35	0.32	0.27	0.17
CaO	31.27	31.69	29.47	31.27	30.74	29.65	29.43	31.53	32.37
TiO_2	0.25	0.34	0.30	0.28	0.29	0.28	0.28	0.24	0.19
V_2O_3	0.03	0.11	0.10	0.10	0.09	0.09	0.09	0.07	0.05
Cr_2O_3	2.75	1.87	2.35	2.14	1.57	2.64	2.25	1.88	1.27
MnO	5.38	6.48	5.80	5.91	5.40	5.23	4.85	3.45	2.51
FeO *	30.46	35.49	38.83	33.71	31.81	31.55	30.35	22.21	16.56
MoO_3	0.05	N/A **	N/A	N/A	N/A	N/A	N/A	N/A	N/A
C	N/A	0.90	1.06	1.35	1.52	1.93	2.59	4.45	4.80
LOI 110 °C	N/A	0.44	0.68	0.74	0.81	0.65	0.77	1.11	1.57
LOI 1000 °C	N/A	0.42	2.04	4.93	7.43	9.03	10.32	16.71	21.99

* Total Fe expressed as FeO. ** Data not available.

3.2. Mineralogical Composition

Eight mineral phases are detected by X-ray diffraction—Wustite (FeO), a spinel solid solution ($(Fe,Mg)(Fe,Mn,Cr)_2O_4$), chromite ($Fe(Cr,Al)_2O_4$), brownmillerite($Ca_2(Fe,Al,Cr)_2O_5$), calcium chromite ($CaCr_2O_4$), larnite (Ca_2SiO_4), calcite ($CaCO_3$) and quartz (SiO_2). The XRD pattern of the finest (<0.25 mm) and the coarsest (>10 mm) fractions are presented in Figure 2. Table 3 presents the relative abundance of these minerals in each fraction estimated by comparing the different XRD patterns. Wustite, brownmillerite and larnite abundances decrease with particle size, while quartz, calcium chromite, spinel solid solution and calcite follow the opposite trend. These two latter minerals are known as possible secondary minerals in slag [15,28], so their presence in fine fractions, which are more prone to weathering, makes sense. On the contrary, wustite brownmillerite and larnite, which are preferentially found in coarse fractions, reflect probably the initial composition of the slag. Quartz which cannot be formed at room temperature and pressure is supposed to come from other materials stored with slag on the site (sand, refractory bricks). This distribution of minerals

among the different fractions must also be related to the disintegration phenomenon that takes place during cooling. It is known that at a certain temperature, slag pieces crumble into a fine powder due to the transformation of dicalcium silicate (larnite) from the polymorph βCa_2SiO_4 to γCa_2SiO_4. This transformation is accompanied by an increase in volume of about 12% and causes the slag pieces to burst [29]. The consequence in the present study is that the larnite particles that undergo this disintegration are found in the fine fractions, and are very quickly transformed into calcite on contact with air and moisture.

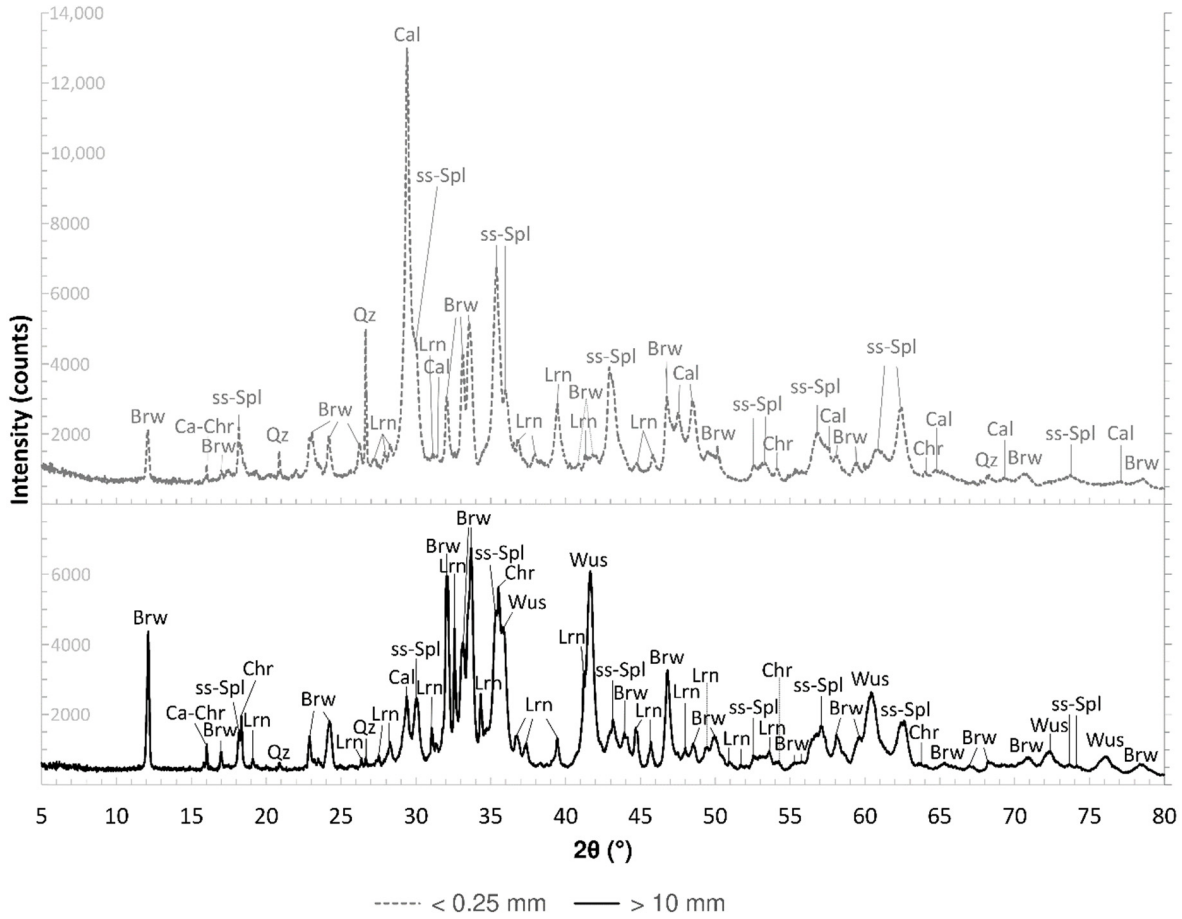

Figure 2. X-ray diffraction (XRD) pattern for the fractions <0.25 mm and >10 mm (Wus = wustite, ss-Spl = spinel solid solution, Chr = chromite, Brw = brownmillerite, Ca-Chr = calcium chromite, Lrn = larnite, Cal = calcite, Qz = quartz).

Table 3. Relative abundance of the different mineral phases detected by XRD in each fraction (- means absent, + present, ++ quite abundant and +++ very abundant).

Phase	Formula	>10 mm	10–5 mm	5–2.5 mm	2.5–1.6 mm	1.6–1.0 mm	1.0–0.5 mm	0.5–0.25 mm	<0.25 mm
Wustite	FeO	+++	++	+	+	+	+	+	-
Spinel solid solution	$(Fe,Mg)(Fe,Mn,Cr)_2O_4$	+	++	+++	+++	+++	+++	+++	+++
Chromite	$Fe(Cr,Al)_2O_4$	++	++	++	++	++	++	++	++
Brownmillerite	$Ca_2(Fe,Al,Cr)_2O_5$	+++	++	++	++	++	++	++	+
Calcium chromite	$CaCr_2O_4$	+	+	+	+	+	+	+	++
Larnite	Ca_2SiO_4	+++	+++	+++	++	++	++	+	+
Calcite	$CaCO_3$	+	+	+	+	+	+	+++	+++
Quartz	SiO_2	-	-	+	+	+	++	++	++

Electron Microprobe analyses coupled with Raman spectroscopy gives further information about mineral composition. Most of the phases detected by XRD are observed, except for quartz and calcite. Quartz has been considered to be a contamination coming from other materials, thus, it is not observed in individual slag grains. Calcite is mainly present in the fine fractions (<0.5 mm) that have not been incorporated into the epoxy blocks. In addition, as a secondary mineral, calcite is expected to be found at the rims of the grains, and so was probably removed by polishing. Tricalcium silicate (Ca_3SiO_5) is detected in addition of larnite (Ca_2SiO_4) according to EMPA (Table 4). It can also be larnite with lime micro-inclusions resulting from the decomposition of tricalcium silicate at 1250 °C during cooling process, as highlighted by Waligora et al. and Engström et al. [14,30].

The most common structures found in the investigated slags are presented in Figure 3. They are almost entirely crystallized in accordance with slow cooling conditions (air-cooling). Some grains present a dendritic texture, indicating a slightly higher cooling rate as in Figure 4a. Calcium silicate particles are generally subhedral with an ovoid shape, while brownmillerite appears as elongated lamellae (Figure 3a,b). Calcium chromite appears as needle shaped minerals, sometimes surrounded by brownmillerite (Figure 3b). The spinel solid solution must be differentiated from chromite which also makes part of the spinel family. Indeed, in the studied samples, chromite crystals are euhedral, and so easily recognizable with their cubic shape, while for the spinel solid solution $(Fe,Mg)(Fe,Mn,Cr)_2O_4$, the grains have a rounded shape (Figure 3a,b) which is reminiscent of the shape of wustite in many studies of EAF slag [7,13]. In addition, a significant number of these grains have a heterogeneous appearance (Figure 4b,c and Figure 5). These observations suggest that this spinel solid solution is actually secondary, and results from an oxidation of a primary wustite solid solution (Fe,Mn,Mg)O. Indeed wustite is known to be metastable [31] and several occurrence of spinel exsolution in wustite are reported in the literature [32,33]. EMPA and Raman analyses below help to understand the heterogeneous nature of the spinel solid solution.

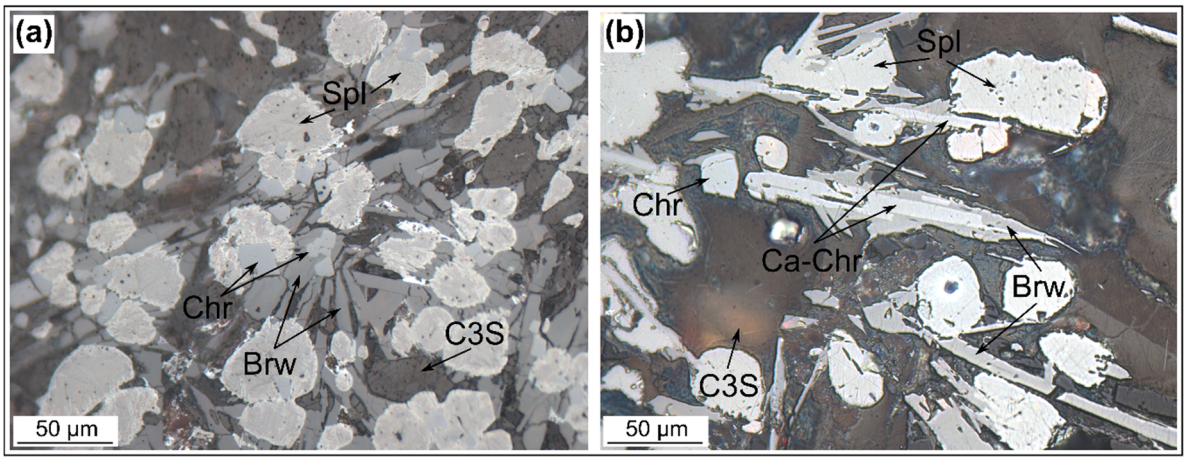

Figure 3. Reflected light microphotographs taken by optic microscope Leica DM4500 P on selected 1 mm grains from sample Mix 1 (**a**) Block 1–grain 25 (**b**) Block 5–grain 16. Abbreviations: spinel solid solution (Spl), chromite (Chr), brownmillerite (Brw), tricalcium silicate (C3S), calcium chromite (Ca-Chr).

The average chemical composition of each mineral phase obtained by EMPA is given in Table 4. All the results for EMPA point analyses are given in Supplementary Material, Table S2. It allows an estimation of the average stoichiometry $(Mg_{0.7}Fe_{0.3})(Fe_{1.5}Mn_{0.5})O_4$ for the spinel solid solution. However, this phase is not homogenous and varies between the end members magnetite (Fe_3O_4)–jacobsite ($Fe(Fe,Mn)_2O_4$) and magnesio-ferrite ($MgFe_2O_4$). Point analyses give Mg, Mn and Fe contents ranging from 0.32 to 43.51 at. %, from 0.96 to 16.12 at. % and from 4.97 to 47.73 at. % respectively.

Table 4. Chemical composition of each mineralogical phase measured by electron microprobe (C3S = alite, C2S = belite (or larnite), Brw = brownmillerite, Chr = chromite, ss-Spl = spinel solid solution, Ca-Chr = calcium chromite).

Element	Mineral Phase	C3S	C2S	Brw	Chr	ss-Spl	Ca-Chr
Mg (at. %)	min–max	0.00–0.10	0.00–0.38	0.12–0.51	5.10–7.50	0.32–43.51	0.29–0.97
	average	0.05	0.03	0.27	6.70	10.96	0.63
	std. Dev.	0.04	0.16	0.13	0.75	9.03	0.28
Al (at. %)	min–max	0.54–1.72	0.15–0.64	2.72–9.46	0.99–5.04	0–2.37	0.33–0.75
	average	0.92	0.34	6.47	2.50	0.20	0.52
	std. Dev.	0.34	0.16	2.13	1.49	0.40	0.20
Si (at. %)	min–max	9.54–10.35	12.69–13.65	0.03–2.12	<DL *	<DL	0.01–0.24
	average	10.01	13.14	0.73	<DL	<DL	0.15
	std. Dev.	0.26	0.36	0.50			0.34
P (at. %)	min–max	0.21–0.55	0.32–1.06	0.00–0.36	<DL	<DL	<DL
	average	0.35	0.68	0.04	<DL	<DL	<DL
	std. Dev.	0.12	0.23	0.07			
Ca (at. %)	min–max	30.32–32.04	26.95–28.31	22.06–24.39	0.37–0.97	0.18–7.49	14.25–16.33
	average	31.36	27.93	23.22	0.60	1.87	14.93
	std. Dev.	0.63	0.47	0.52	0.23	2.01	0.73
Ti (at. %)	min–max	<DL	<DL	0.04–1.55	0.02–0.08	<DL	<DL
	average	<DL	<DL	0.70	0.04	<DL	<DL
	std. Dev.			0.33	0.02		
V (at. %)	min–max	<DL	<DL	0.04–0.98	0.03–0.13	<DL	<DL
	average	<DL	<DL	0.18	0.06	<DL	<DL
	std. Dev.			0.19	0.04		
Cr (at. %)	min–max	<DL	<DL	0.22–6.64	21.77–26.63	0–6.38	22.43–25.10
	average	<DL	<DL	3.39	24.88	0.94	24.43
	std. Dev.			1.79	1.74	1.23	1.03
Mn (at. %)	min–max	0.27–0.74	0.03–0.47	0.24–1.26	2.65–5.70	0.96–16.12	0.06–0.24
	average	0.46	0.14	2.59	3.50	8.43	0.12
	std. Dev.	0.16	0.15	0.24	0.91	3.53	0.07
Fe (at. %)	min–max	0.90–1.46	0.25–0.91	5.20–17.13	2.47–7.39	4.97–47.73	2.48–3.36
	average	1.18	0.40	11.13	4.80	27.23	2.79
	std. Dev.	0.16	0.23	3.95	1.21	8.66	0.32
Number of analyses		9	7	24	12	81	6

* below the detection limit.

The diversity of the spinel solid solution particles is illustrated in Figures 4 and 5. Four typical forms are presented:

- Intergrowth of jacobsite (Figure 4a, points 1, 2 and 4) with calcium-silicate (point 3). Chemical compositions measured at the points 1 and 2 are given in Table 5.
- Particles with patchy zonations. On Figure 4b, three different phases are actually distinguishable within the same particle: Fe rich jacobsite (points 5 and 6), jacobsite (points 7 and 8) and harmunite, $CaFe_2O_4$ (points 9 and 10) based on the work of Galuskina et al. [34]. Some hematite peaks visible on Raman spectra for point 8 suggest that the corresponding phase is partially oxidized (Figure 4d). However, this oxidation may be caused by Raman laser heating [35,36].
- Partially oxidized jacobsite (identified as Mg-Mn rich maghemite) with harmunite exsolutions. On Figure 4c, mottled areas correspond to the Mg-Mn rich maghemite (points 11, 12 and 15) according to Raman spectrum (Figure 4f) and EMPA point analyses (Table 5). Grey lamellae are identified as exsolved harmunite thanks to EMPA (Table 5), however it could not be confirmed with Raman analyses since the laser beam was to large. Thin light borders around the lamellae may be pure magnetite or wustite.
- Grains with Mg and Mn zonations. For example, in Figure 5, Mg content decreases gradually from the centre of the grain to the edge (Figure 5h), while Mn content follows the opposite trend (Figure 5f) Fe content is slightly higher at the extreme edge (Figure 5e). Some needle shaped minerals are included in the grains, composed of Ca and Cr at the centre of the grain (Figure 5b,g) and Ca, Fe and Mn at the edge (Figure 5b,e,f).

In conclusion, various chemical zonations, harmunite exsolutions and maghemite are highlighted thanks to EMPA and Raman analyses explaining most of the heterogeneity observed. Wustite is not clearly identified whereas it is detected by XRD. This primary phase can however reside in very fine intergrowths for which it is very difficult to carry out a single-phase analysis without contamination from the adjacent phases.

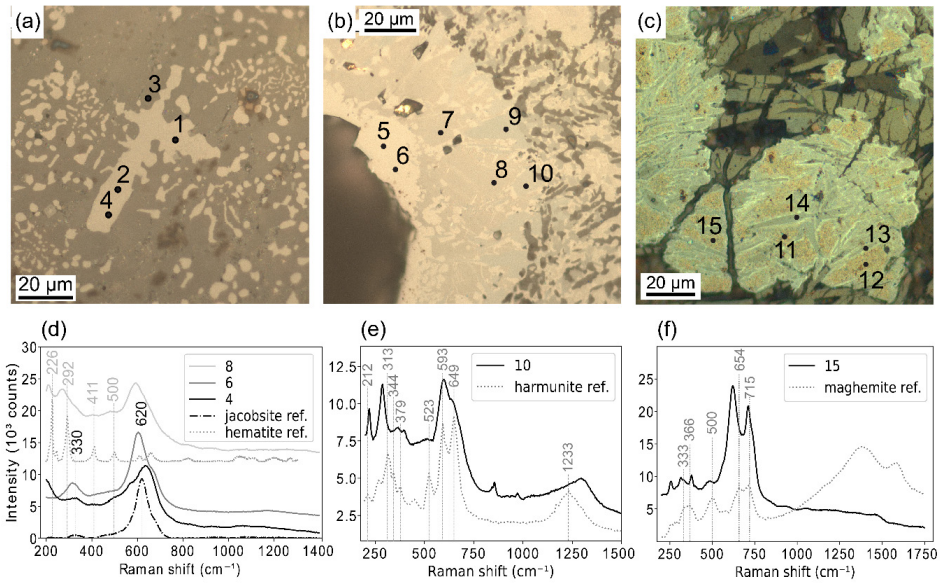

Figure 4. (**a**–**c**) Reflected light microphotographs taken by optic microscope Leica DM4500 P on selected 1 mm grains from sample Mix 1: (**a**) Block 1–grain 27 (**b**) Block 4–grain 16 (**c**) Block 5–grain 02. (**d**) Raman spectra referring to the points number 4, 6 and 8. Reference spectra were taken from the RRUFF database for jacobsite (Jakobsberg, Sweden) and hematite (Argentina). (**e**) Raman spectrum referring to the point number 10. Reference spectrum for harmunite was taken from Galuskina et al. [34]. (**f**) Raman spectrum referring to the point number 15. Reference spectrum for maghemite was taken from De Faria et al. [37].

Table 5. Chemical composition (wt. %) obtained by EMPA on the points number 1, 2, 3, 5, 7, 8, 9, 11, 12, 13 and 14 in Figure 4a–c.

Point Number	Mg (at. %)	Al (at. %)	Si (at. %)	Ca (at. %)	Cr (at. %)	Mn (at. %)	Fe (at. %)	Identified Mineral
1	14.32	0.90	0.02	0.50	1.69	8.81	23.03	jacobsite
2	13.85	0.39	0.03	0.60	1.29	9.06	24.28	jacobsite
3	0.38	0.64	12.69	26.95	0.04	0.47	0.91	larnite
5	1.35	0.00	0.02	0.43	0.00	5.11	43.09	jacobsite
7	6.11	0.10	0.02	0.43	0.02	9.97	33.35	jacobsite
8	4.62	0.15	0.03	2.63	0.06	7.21	35.27	jacobsite
9	0.75	0.13	0.01	11.31	0.16	2.12	35.32	harmunite
11	18,00	0.00	0.02	0.50	0.44	10.68	20.14	maghemite
12	11.20	0.03	0.00	2.06	0.66	8.98	26.90	maghemite
13	5.45	0.02	0.02	12.47	1.53	4.96	25.15	harmunite
14	0.18	0.12	0.01	21.74	3.47	1.18	22.3	harmunite

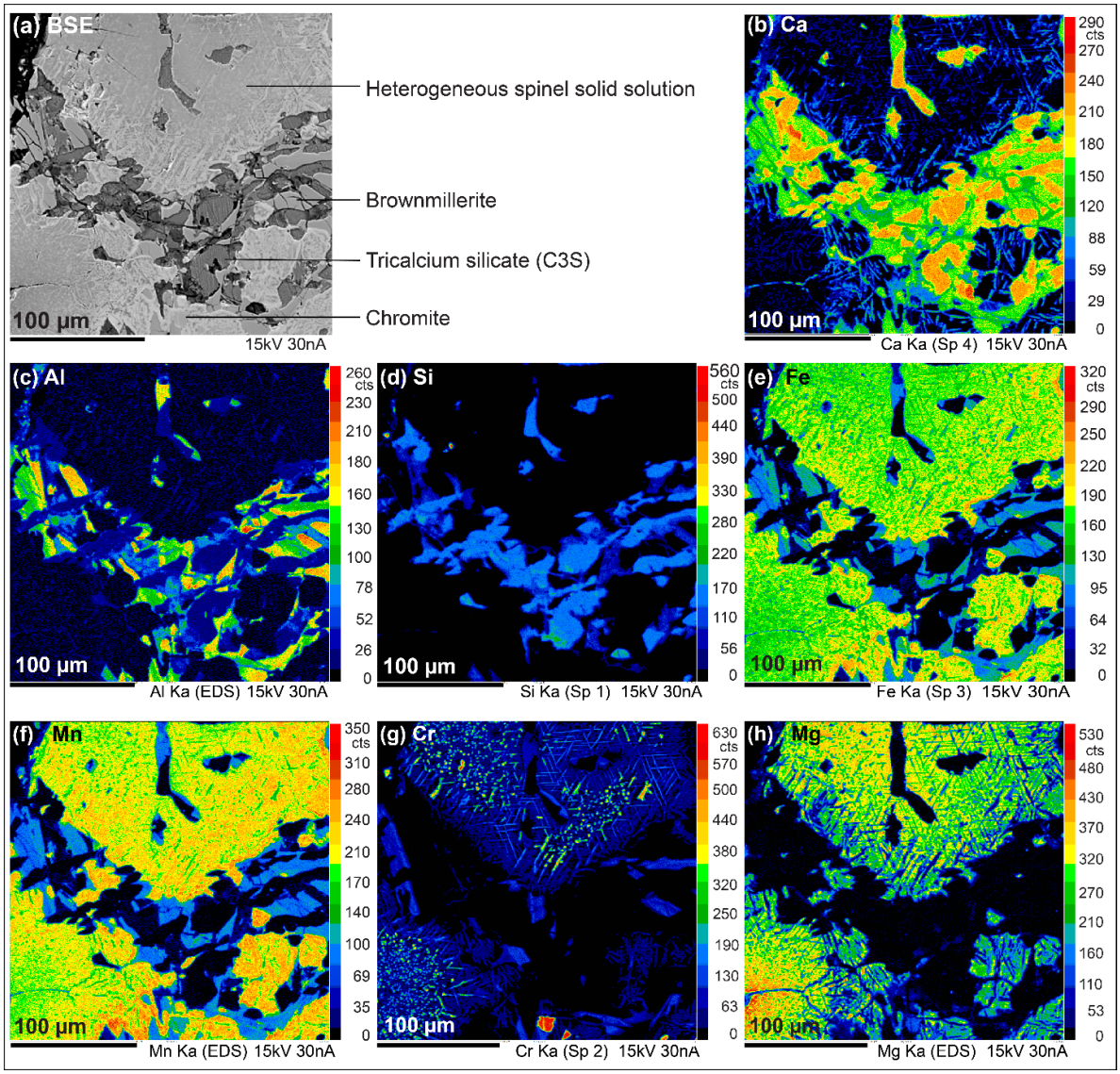

Figure 5. Chemical maps of a selected 1 mm grain from sample Mix 1 (Block 5 grain 07). (**a**) BSE (back-scattered electrons) image; (**b**–**h**) quantified chemical maps of Ca, Al, Si, Fe, Mn, Cr, and Mg obtained by EMPA.

3.3. Potential Hazardous Metal Location

Three potential hazardous metals are identified—Chromium (Cr), molybdenum (Mo) and vanadium (V). EMPA results presented in Table 4 give the concentration of these metals in each mineral phase. It shows that the main chromium bearing minerals are chromite with an average of 24.88 at. % and calcium chromite with an average of 24.43 at. %. Cr is also present in brownmillerite (3.39 at. %) and in a lesser extend in the spinel solid solution $(Mg,Fe)(Fe,Mn)_2O_4$ (0.94 at. %). V is present in small amounts in brownmillerite (up to 0.98 at. %) and in chromite (up to 0.13 at. %). Mo contents measured by EMPA are below detection limit, so this element is not clearly localized.

3.4. Focus on Magnetic Phases

Magnetic based techniques helped to complete the study about iron oxides. The studied slags present very high magnetic susceptibility values, ranging from 47.74×10^{-6} m^3/kg to 77.27×10^{-6} m^3/kg, with an average of 59.15×10^{-6} m^3/kg, showing the presence of ferromagnetic minerals s.l. (i.e., ferromagnetic or ferrimagnetic) such as magnetite or jacobsite. Magnetite is known to have magnetic susceptibility values near 580×10^{-6} m^3/kg [38] and the magnetic susceptibility of jacobsite can reach 1.09×10^{-1} $CGSM/cm^3$ (i.e., 270×10^{-6} m^3/kg given a density of 4990 kg/m^3 for jacobsite) [39]. Magnetic susceptibility of the surrounding rocks is much lower. A value of 121.20×10^{-9} m^3/kg is obtained for micaschiste, 87.55×10^{-9} m^3/kg for gneiss and 29.35×10^{-9} m^3/kg for coarse sandstone.

In a more global context, Figure 6 shows the studied slag magnetic susceptibilities among other values reported for various materials—dust loaded tree leaves [40–42], urban dust (air suspended particles and road dust) [43,44], industrial wastes [21–24], rocks [45,46] and soils [17,18,24,47–51]. Values measured for the surrounding rocks are also reported. It is interesting to note that the measured slag magnetic susceptibilities are in the upper end of values corresponding to urban dusts and industrial wastes and match the highest values reported for rocks (77×10^{-6} m^3/kg for porphyry and 65×10^{-6} m^3/kg for andesite [45]). A value of 95.333×10^{-6} m^3/kg was measured for air suspended particles [43]. Only one much higher value was reported for industrial waste (152.965×10^{-6} m^3/kg measured on lagooned ash [22]), while the other studied wastes peak at 90.73×10^{-6} m^3/kg with fly ash [24]. Magnetic susceptibility of the studied slag is also significantly higher than for soils (maximum of 31.25×10^{-6} m^3/kg in an industrial area [17]) and tree leaves (maximum of 0.54×10^{-6} m^3/kg for Himalayan cypress leaves in Kathmandu [40]).

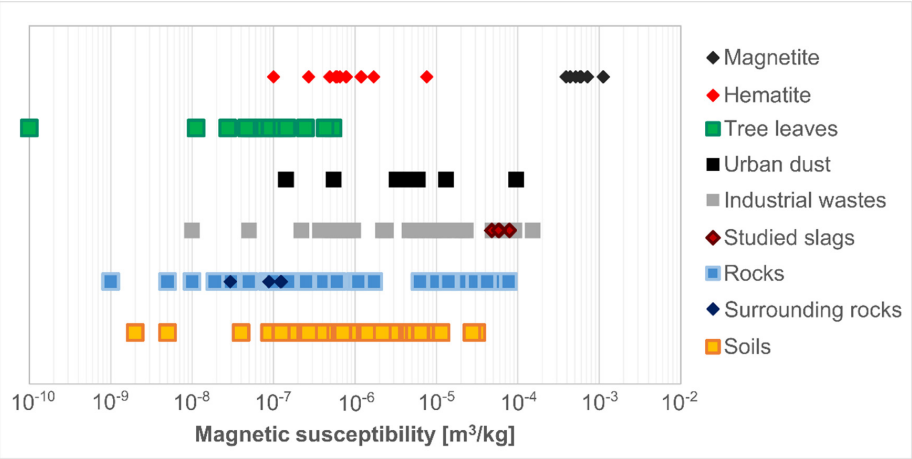

Figure 6. Mass magnetic susceptibility of steel making slag among various materials, 132 values are reported according to the references [17,18,21–24,38,40–52]. Magnetic susceptibility measured for some surrounding rocks (micaschiste, gneiss, sandstone) are included. Hematite and magnetite usual susceptibilities are given as points of reference: the wide range of values is explained by the fact that magnetic susceptibility depends on the size and shape of the crystals, and on the presence of trace elements [38,52].

The evolution of magnetic susceptibility as a function of temperature for the sample Mix-1 is shown in Figure 7. This thermomagnetic curve shows a peak of κ around −155 °C which corresponds to the Verwey transition and a drop around 575 °C, the Curie temperature both indicating the presence of magnetite (Fe_3O_4). This means that the spinel solid solution $(Mg,Fe)(Fe,Mn)_2O_4$ takes the form of rather pure magnetite in some cases. Indeed, the Verwey transition is detectable only for magnetite, and the Curie temperature is very sensitive to stoichiometry, so the other forms of magnetic spinel will manifest themselves at different temperatures. The Curie temperatures of the end members jacobsite $MnFe_2O_4$ and magnesio-ferrite $MgFe_2O_4$ are respectively 310 °C and 440 °C [53]. The progressive decrease of κ between 280 °C and 557 °C in Figure 7 shows that a wide range of the intermediary phases between jacobsite, magnesio-ferrite and magnetite are present in the studied slag. The loss of approximately 70% of the initial magnetic susceptibility between 280 °C and 557 °C indicates that the jacobsite–magnesio-ferrite solid solution is mostly responsible for the magnetic behaviour of the slag. Pure magnetite was not clearly observed by electron microprobe and should therefore be present in only very small quantities. The irreversibility of the curve must be pointed out. The production of thermomagnetic curves (heating and cooling) from room temperature to 200 °C and from room temperature to 400 °C shows that reversibility is lost from 300 °C onwards, indicating a phase transformation near this temperature that could be caused by dehydration.

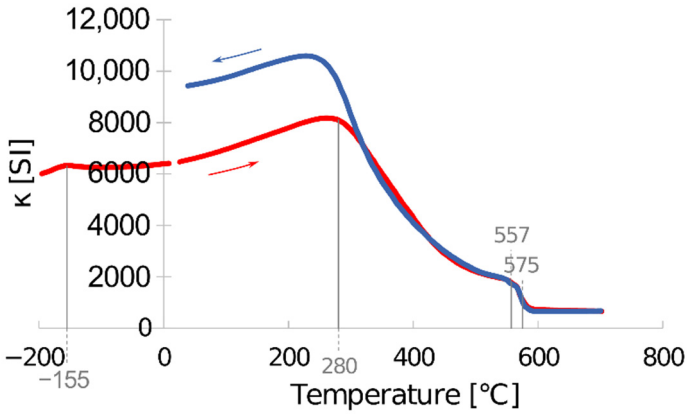

Figure 7. Variation of the magnetic susceptibility (κ) during heating-cooling cycle (red and blue line respectively) from −192 °C to room temperature and from room temperature to 700 °C.

3.5. Principal Component Analysis

The correlation circle resulting from PCA is shown on Figure 8. It gives a projection of the eight initial variables as a function of the first two principal components, dimension 1 and dimension 2, which bear respectively 39.30% and 18.77% of the total variance. Magnetic susceptibility is obviously correlated with FeO content. Another strong correlation appears between MnO, Cr_2O_3 and V_2O_3 contents. More broadly, FeO, MnO, Cr_2O_3 and V_2O_3 contents seem to behave in the same way. Thus, magnetic susceptibility seems to be an indicator for high contents in MnO, Cr_2O_3 and V_2O_3, in addition to FeO. The contents in CaO and MgO are also correlated, while CaO is anticorrelated with SiO_2. Al_2O_3 is anticorrelated with FeO and Cr_2O_3. No obvious correlation appears for the contents in MoO_3.

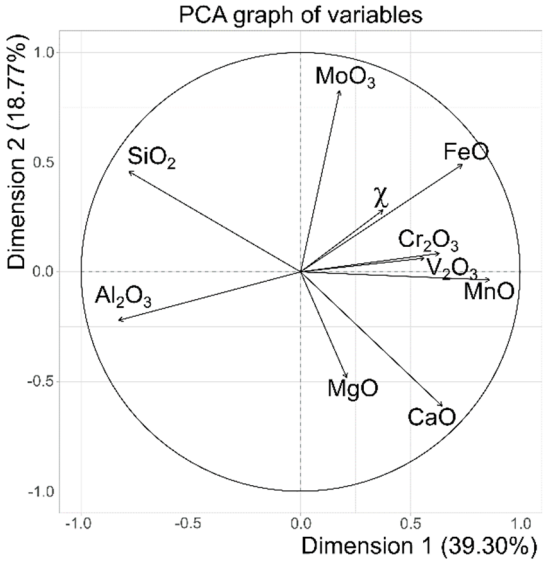

Figure 8. Correlation circle obtained from Principal Component Analysis (χ = mass magnetic susceptibility).

4. Discussion

4.1. Comparison with Other EAF Slag

The studied slags have quite a high CaO/SiO_2 ratio, with an average of 3.15, while in previous studies focusing on EAF slag, it typically ranged from 0.9 to 2.9 [5,7,8,15,54–59]. Consequently, the little amount of Si present is only found in calcium silicates, the other silicate minerals usually found in slag such as gehlenite, fayalite or kirschsteinite are absent. The remaining Ca is associated with Fe, Al and Cr to form brownmillerite and in a lesser extent calcium chromite and calcium ferrite (harmunite). The presence of these two latter minerals is not common in EAF slag and appears as a specificity of very basic slag. Calcium chromite occurrences were mentioned by Albertsson et al., Cabrera-Real et al. and Mombelli et al. [6,7,60] and was shown to be favoured in highly alkaline slag. The distribution of the mineral phases between the different grain size fractions gives an idea on how the material breaks up over time. It appears that ferrous minerals (wustite, brownmillerite, chromite), which are more resistant, are concentrated in the coarsest fractions, while calcium silicates tend to disintegrate and form calcite. Some studies outlined that calcite thus formed on the surface of slag particle can have a protective effect and limit the leaching of hazardous metals [15,61]. This applies only if the material does not undergo further fragmentation due to natural alteration or any manipulation.

4.2. Hazardous Metals Location and Potential Mobility

This study focuses on three potential hazardous metals—Cr, Mo and V. Cr is usually present as Cr (III) and Cr (VI) in the environment. Cr (III) is poorly soluble unlike Cr (VI) which has a high mobility and is known to be highly toxic [62,63]. Mo and V play an essential role in biological systems, but have a negative effect on organisms above a certain concentration [64–66]. V interfere with the function of P-containing biomolecules [65], and Mo can be adsorbed in soils and accumulated in plants, causing ruminants disease such as molybdenosis [67,68]. The contents of these two metals being very low in the studied slag, the main concerns are about Cr which has been found in chromite, calcium chromite, brownmillerite and in a lesser extent in the spinel solid solution $(Mg,Fe)(Fe,Mn)_2O_4$. In these phases, it is expected to be present in its less toxic form Cr (III), but it can react on cooling with free CaO and form Cr (VI) as described by Lee and Nassaralla [69]. Albertsson et al., Cabrera-Real et al. and Mombelli et al. [6,7,60] showed that this element is hardly leachable when dissolved in spinel minerals but could be released by calcium chromite and brownmillerite. This latter mineral also contains up to 0.98 at. % of V, and could release this metal at the same time. De Windt et al. [28]

mention an incongruent dissolution of brownmillerite in Basic Oxygen Furnace slag—Al and V are leached while Ca, Fe and Cr remain forming dicalcium ferrite.

4.3. Hazardous Metals and Magnetic Susceptibility

The global correlation between magnetic susceptibility, Fe, Cr, V, and Mn obtained with the PCA is consistent since these elements are present in significant amounts in chromite and in the spinel solid solution, except for V which is mainly found in brownmillerite. Magnetic susceptibility is mainly due to the spinel solid solution which has been identified as ferromagnetic. Whereas the amount of Fe in chromite is too low to give ferromagnetic properties to chromite. Indeed, Ziemniak and Castelli [70] showed that the solid solution $Fe(Fe_{1-n}Cr_n)_2O_4$ is paramagnetic at room temperature if $n \geq 0.65$. According to EMPA analysis, the studied chromite formula would be close to $(Fe_{0.3},Mg_{0.5},Mn_{0.2})(Al_{0.1},Cr_{0.9})_2O_4$, so with n = 0.9, the magnetic susceptibility should be much lower than for magnetite and for the spinel solid solution $(Mg,Fe)(Fe,Mn)_2O_4$. Thus, magnetic susceptibility appears as an indicator for high contents in Fe, Mn, Cr and V in the studied slag, because chromite and the spinel solid solution seem to be associated. Mo has not been detected in a particular phase and is supposed to be disseminated in all minerals, which would be in accordance with the PCA showing no correlation with any other variable. Some precautions must be taken about V and Mo since the contents are very low the significance of the correlations can be questioned for these elements.

4.4. Magnetic Susceptibility as a Field Tool

The very high susceptibility of the studied slag makes this material easily distinguishable from soils, rocks or other wastes. Magnetic measurements are quick and can be easily carried out on the field scale. Magnetic susceptibility could be used as a tool to detect the dispersion of slag particles in soils or in sediments, or to delineate historical slagheaps areas, especially when the history of the site is little known. The use of magnetic susceptibility as a tracer for heavy metals (Cr, V) seems possible according to the correlations obtained by PCA, but it needs to be tested at a larger scale. It could help to identify the highest concentrations spots before a more detailed study.

5. Conclusions

In this work, partially weathered EAF slag samples are studied, with a multi-analytical approach combining chemical, mineralogical and magnetic techniques. The material is characterised by a high CaO/SiO_2 ratio compared to other EAF slags. It contains several potentially hazardous metals—Cr, Mo and V. Mineralogical analyses reveal that Cr is mainly present in two minerals—chromite, which is rather stable and Ca-chromite, which is much more soluble. Mo and V are present in very low quantities but their leachability should be controlled.

Magnetic measurements show a very high magnetic susceptibility compared to other industrial wastes, it is explained by the presence of the spinel solid solution $(Mg,Fe)(Fe,Mn)_2O_4$ and some magnetite. Magnetic techniques are easily transposable to the field scale and must be considered when estimating the dispersal of slag particles in the environment.

Coupling chemical and magnetic analyses is interesting but does not exclude a detailed study of the mineralogy. It is important to keep in mind that the hazardous levels of these metals depends not only on their concentrations, but also on their speciation and the solubility of their host minerals. In this study, a Principal Component Analysis shows a correlation between magnetic susceptibility and Fe with the metals Cr, Mn and V. It means that samples richer in ferromagnetic minerals are also richer in Cr and V bearing minerals. It must be assessed at the field scale in future studies.

Supplementary Materials: The following are available online at http://www.mdpi.com/2075-163X/10/8/705/s1, Table S1: Bulk chemical analyses and magnetic susceptibilities obtained for the samples slag-1A to slag-30B, Table S2: Results of the performed EMPA point analyses.

Author Contributions: Conceptualization, M.H., J.B., V.L. and D.G.; methodology, M.H., J.B., V.L. and D.G.; validation, J.B., V.L., D.G., M.B., S.P. and J.-P.B.; formal analysis, M.H., J.B., V.L., D.G., M.B. and S.P.; investigation,

M.H., J.B., V.L. and D.G.; data curation, M.H., M.B., S.P.; writing—original draft preparation M.H.; writing—review and editing, M.H., J.B., V.L., D.G., M.B., S.P. and J.-P.B.; visualization, M.H.; supervision, J.B., V.L., D.G. and J.-P.B.; project administration, J.B., V.L. and D.G.; funding acquisition, J.B., V.L. and D.G. All authors have read and agreed to the published version of the manuscript.

Funding: This research received no external funding.

Acknowledgments: The authors would like to thank Colette Guibauld (Laboratoire Magmas et Volcans, Saint-Etienne) for the polished sections preparation, Olivier Valfort (Ecole des Mines de Saint-Etienne) for X-ray diffraction analyses and Jean-Luc Devidal (Laboratoire Magmas et Volcans, Clermont-Ferrand) for electron microprobe analyses. We also acknowledge Frédéric Astolfi (ArcelorMittal) for facilitating the access to the slag heap of Châteauneuf.

Conflicts of Interest: The authors declare no conflict of interest. The funders had no role in the design of the study; in the collection, analyses, or interpretation of data; in the writing of the manuscript, or in the decision to publish the results.

References

1. World Steel Association Steel Industry Co-products. Available online: https://www.worldsteel.org/en/dam/jcr:1b916a6d-06fd-4e84-b35d-c1d911d18df4/Fact_By-products_2016.pdf (accessed on 13 January 2020).
2. Piatak, N.M.; Parsons, M.B.; Seal, R.R. Characteristics and environmental aspects of slag: A review. *Appl. Geochem.* **2015**, *57*, 236–266. [CrossRef]
3. European Slag Association (EUROSLAG) Statistical Data. Available online: https://www.euroslag.com/research-library-downloads/downloads/ (accessed on 13 January 2020).
4. Council of the European Union Council Directive 1999/31/EC 26 on the Landfill of Waste. 26 April 1999.
5. Lekakh, S.N.; Rawlins, C.H.; Robertson, D.G.C.; Richards, V.L.; Peaslee, K.D. Kinetics of Aqueous Leaching and Carbonization of Steelmaking Slag. *Metall. Mater. Trans. B* **2008**, *39*, 125–134. [CrossRef]
6. Albertsson, G.J.; Engström, F.; Teng, L. Effect of the Heat Treatment on the Chromium Partition in Cr-Containing Industrial and Synthetic Slags. *Steel Res. Int.* **2014**, *85*, 1418–1431. [CrossRef]
7. Mombelli, D.; Mapelli, C.; Barella, S.; Di Cecca, C.; Le Saout, G.; Garcia-Diaz, E. The effect of microstructure on the leaching behaviour of electric arc furnace (EAF) carbon steel slag. *Process Saf. Environ. Prot.* **2016**, *102*, 810–821. [CrossRef]
8. Neuhold, S.; van Zomeren, A.; Dijkstra, J.J.; van der Sloot, H.A.; Drissen, P.; Algermissen, D.; Mudersbach, D.; Schüler, S.; Griessacher, T.; Raith, J.G.; et al. Investigation of Possible Leaching Control Mechanisms for Chromium and Vanadium in Electric Arc Furnace (EAF) Slags Using Combined Experimental and Modeling Approaches. *Minerals* **2019**, *9*, 525. [CrossRef]
9. Tossavainen, M.; Engstrom, F.; Yang, Q.; Menad, N.; Lidstrom Larsson, M.; Bjorkman, B. Characteristics of steel slag under different cooling conditions. *Waste Manag.* **2007**, *27*, 1335–1344. [CrossRef]
10. Tsakiridis, P.E.; Papadimitriou, G.D.; Tsivilis, S.; Koroneos, C. Utilization of steel slag for Portland cement clinker production. *J. Hazard. Mater.* **2008**, *152*, 805–811. [CrossRef]
11. Loncnar, M.; Mladenovic, A.; Zupancic, M.; Bukovec, P. Comparison of the mineralogy and microstructure of EAF stainless steel slags with reference to the cooling treatment. *J. Min. Met. B Met.* **2017**, *53*, 19–29. [CrossRef]
12. Yildirim, I.Z.; Prezzi, M. Chemical, Mineralogical, and Morphological Properties of Steel Slag. *Adv. Civ. Eng.* **2011**, *2011*, 1–13. [CrossRef]
13. Neuhold, S.; Algermissen, D.; Drissen, P.; Adamczyk, B.; Presoly, P.; Sedlazeck, K.P.; Schenk, J.; Raith, J.G.; Pomberger, R.; Vollprecht, D. Tailoring the FeO/SiO_2 Ratio in Electric Arc Furnace Slags to Minimize the Leaching of Vanadium and Chromium. *Appl. Sci.* **2020**, *10*, 2549. [CrossRef]
14. Engström, F.; Adolfsson, D.; Yang, Q.; Samuelsson, C.; Björkman, B. Crystallization Behaviour of some Steelmaking Slags. *Steel Res. Int.* **2010**, *81*, 362–371. [CrossRef]
15. Engström, F.; Larsson, M.L.; Samuelsson, C.; Sandström, Å.; Robinson, R.; Björkman, B. Leaching Behavior of Aged Steel Slags. *Steel Res. Int.* **2014**, *85*, 607–615. [CrossRef]
16. Rosowiecka, O.; Nawrocki, J. Assessment of soils pollution extent in surroundings of ironworks based on magnetic analysis. *Studia Geophys. Geod.* **2010**, *54*, 185–194. [CrossRef]
17. Cao, L.; Appel, E.; Hu, S.; Yin, G.; Lin, H.; Rösler, W. Magnetic response to air pollution recorded by soil and dust-loaded leaves in a changing industrial environment. *Atmos. Environ.* **2015**, *119*, 304–313. [CrossRef]

18. Girault, F.; Perrier, F.; Poitou, C.; Isambert, A.; Théveniaut, H.; Laperche, V.; Clozel-Leloup, B.; Douay, F. Effective radium concentration in topsoils contaminated by lead and zinc smelters. *Sci. Total Environ.* **2016**, *566–567*, 865–876. [CrossRef]
19. Attoucheik, L.; Jordanova, N.; Bayou, B.; Lagroix, F.; Jordanova, D.; Maouche, S.; Henry, B.; Boutaleb, A. Soil metal pollution from former Zn–Pb mining assessed by geochemical and magnetic investigations: case study of the Bou Caid area (Tissemsilt, Algeria). *Environ. Earth Sci.* **2017**, *76*. [CrossRef]
20. Golden, N.; Zhang, C.; Potito, A.P.; Gibson, P.J.; Bargary, N.; Morrison, L. Impact of grass cover on the magnetic susceptibility measurements for assessing metal contamination in urban topsoil. *Environ. Res.* **2017**, *155*, 294–306. [CrossRef]
21. Gołuchowska, B.; Strzyszcz, Z.; Kusza, G. Magnetic Susceptibility and Heavy Metal Content in Dust from the Lime Plant and the Cement Plant in Opole Voivodeship. *Arch. Environ. Prot.* **2012**, *38*, 71–80. [CrossRef]
22. Jordanova, D.; Jordanova, N.; Hoffmann, V. Magnetic mineralogy and grain-size dependence of hysteresis parameters of single spherules from industrial waste products. *Phys. Earth Planet. Inter.* **2006**, *154*, 255–265. [CrossRef]
23. Magiera, T.; Gołuchowska, B.; Jabłońska, M. Technogenic Magnetic Particles in Alkaline Dusts from Power and Cement Plants. *Waterairsoil Pollut.* **2013**, *224*. [CrossRef]
24. Szuszkiewicz, M.; Magiera, T.; Kapička, A.; Petrovský, E.; Grison, H.; Gołuchowska, B. Magnetic characteristics of industrial dust from different sources of emission: A case study of Poland. *J. Appl. Geophys.* **2015**, *116*, 84–92. [CrossRef]
25. Walach, G.; Scholger, R.; Cech, B. Geomagnetic and Geoelectric Prospection on a Roman Iron Production Facility in Hüttenberg, Austria (*Ferrum Noricum*): Geophysical Prospection in Hüttenberg, Austria. *Archaeol. Prospect.* **2011**, *18*, 149–158. [CrossRef] [PubMed]
26. Humphris, J.; Carey, C. New methods for investigating slag heaps: Integrating geoprospection, excavation and quantitative methods at Meroe, Sudan. *J. Archaeol. Sci.* **2016**, *70*, 132–144. [CrossRef]
27. Földvári, M. *Handbook of Thermogravimetric System of Minerals and Its Use in Geological Practice*; Occasional papers of the Geological Institute of Hungary; Geological Inst. of Hungary: Budapest, Hungary, 2011; ISBN 978-963-671-288-4.
28. De Windt, L.; Chaurand, P.; Rose, J. Kinetics of steel slag leaching: Batch tests and modeling. *Waste Manag.* **2011**, *31*, 225–235. [CrossRef]
29. Durinck, D.; Engström, F.; Arnout, S.; Heulens, J.; Jones, P.T.; Björkman, B.; Blanpain, B.; Wollants, P. Hot stage processing of metallurgical slags. *Resour. Conserv. Recycl.* **2008**, *52*, 1121–1131. [CrossRef]
30. Waligora, J.; Bulteel, D.; Degrugilliers, P.; Damidot, D.; Potdevin, J.L.; Measson, M. Chemical and mineralogical characterizations of LD converter steel slags: A multi-analytical techniques approach. *Mater. Charact.* **2010**, *61*, 39–48. [CrossRef]
31. Estrader, M.; López-Ortega, A.; Golosovsky, I.V.; Estradé, S.; Roca, A.G.; Salazar-Alvarez, G.; López-Conesa, L.; Tobia, D.; Winkler, E.; Ardisson, J.D.; et al. Origin of the large dispersion of magnetic properties in nanostructured oxides: Fe_xO/Fe_3O_4 nanoparticles as a case study. *Nanoscale* **2015**, *7*, 3002–3015. [CrossRef]
32. Hazen, R.M.; Jeanloz, R. Wüstite ($Fe_{1-x}O$): A review of its defect structure and physical properties. *Rev. Geophys.* **1984**, *22*, 37. [CrossRef]
33. Wang, Y.G.; Ping, D.H.; Guo, J.G. High-resolution transmission-electron-microscopy observation of the ultra-fine structure of natural magnetite. *J. Appl. Cryst.* **1994**, *27*, 96–102. [CrossRef]
34. Galuskina, I.O.; Vapnik, Y.; Lazic, B.; Armbruster, T.; Murashko, M.; Galuskin, E.V. Harmunite $CaFe_2O_4$: A new mineral from the Jabel Harmun, West Bank, Palestinian Autonomy, Israel. *Am. Mineral.* **2014**, *99*, 965–975. [CrossRef]
35. Dariz, P.; Schmid, T. Ferruginous phases in 19th century lime and cement mortars: A Raman microspectroscopic study. *Mater. Charact.* **2017**, *129*, 9–17. [CrossRef]
36. Shebanova, O.N.; Lazor, P. Raman study of magnetite (Fe_3O_4): Laser-induced thermal effects and oxidation. *J. Raman Spectrosc.* **2003**, *34*, 845–852. [CrossRef]
37. De Faria, D.L.A.; Venâncio Silva, S.; De Oliveira, M.T. Raman microspectroscopy of some iron oxides and oxyhydroxides. *J. Raman Spectrosc.* **1997**, *28*, 873–878. [CrossRef]
38. Dunlop, D.J.; Özdemir, Ö. Magnetizations in Rocks and Minerals. In *Treatise on Geophysics*; Elsevier: Amsterdam, The Netherlands, 2015; pp. 255–308. ISBN 978-0-444-53803-1.

39. Kropáček, V.; Krs, M. Distribution of the values of natural remanent magnetization and magnetic susceptibility of some minerals. *Stud. Geophys. Geod.* **1971**, *15*, 340–352. [CrossRef]
40. Gautam, P.; Blaha, U.; Appel, E. Magnetic susceptibility of dust-loaded leaves as a proxy of traffic-related heavy metal pollution in Kathmandu city, Nepal. *Atmos. Environ.* **2005**, *39*, 2201–2211. [CrossRef]
41. Lehndorff, E.; Urbat, M.; Schwark, L. Accumulation histories of magnetic particles on pine needles as function of air quality. *Atmos. Environ.* **2006**, *40*, 7082–7096. [CrossRef]
42. Moreno, E.; Sagnotti, L.; Dinarès-Turell, J.; Winkler, A.; Cascella, A. Biomonitoring of traffic air pollution in Rome using magnetic properties of tree leaves. *Atmos. Environ.* **2003**, *37*, 2967–2977. [CrossRef]
43. Gargiulo, J.D.; Kumar, R.S.; Chaparro, M.A.E.; Chaparro, M.A.E.; Natal, M.; Rajkumar, P. Magnetic properties of air suspended particles in thirty eight cities from south India. *Atmos. Pollut. Res.* **2016**, *7*, 626–637. [CrossRef]
44. Jordanova, D.; Jordanova, N.; Petrov, P. Magnetic susceptibility of road deposited sediments at a national scale—Relation to population size and urban pollution. *Environ. Pollut.* **2014**, *189*, 239–251. [CrossRef]
45. Hunt, C.P.; Moskowitz, B.M.; Banerjee, S.K. Magnetic Properties of Rocks and Minerals. In *Rock Pysics and Phase Relations A Handbook of Physical Constants*; American Geophysical Union: Washington, DC, USA, 1995; Volume 3, pp. 189–204. ISBN 0-87590-853-5.
46. Hodel, F.; Macouin, M.; Triantafyllou, A.; Carlut, J.; Berger, J.; Rousse, S.; Ennih, N.; Trindade, R.I.F. Unusual massive magnetite veins and highly altered Cr-spinels as relics of a Cl-rich acidic hydrothermal event in Neoproterozoic serpentinites (Bou Azzer ophiolite, Anti-Atlas, Morocco). *Precambrian Res.* **2017**, *300*, 151–167. [CrossRef]
47. Hanesch, M.; Scholger, R. Mapping of heavy metal loadings in soils by means of magnetic susceptibility measurements. *Environ. Geol.* **2002**, *42*, 857–870. [CrossRef]
48. Jakšík, O.; Kodešová, R.; Kapička, A.; Klement, A.; Fér, M.; Nikodem, A. Using magnetic susceptibility mapping for assessing soil degradation due to water erosion. *Soil Water Res.* **2016**, *11*, 105–113. [CrossRef]
49. Jordanova, N.; Jordanova, D.; Petrov, P. Soil magnetic properties in Bulgaria at a national scale—Challenges and benefits. *Glob. Planet. Chang.* **2016**, *137*, 107–122. [CrossRef]
50. Martin, A.P.; Ohneiser, C.; Turnbull, R.E.; Strong, D.T.; Demler, S. Soil magnetic susceptibility mapping as a pollution and provenance tool: an example from southern New Zealand. *Geophys. J. Int.* **2018**, *212*, 1225–1236. [CrossRef]
51. Panaiotu, C.G.; Necula, C.; Panaiotu, C.E.; Axente, V. A magnetic investigation of heavy metals pollution in Bucharest. In *Sustainability for Humanity & Environment in the Extended Connection Field Science-Economy-Policy, Scientific Reunion of the Special Program of Alexander von Humbold Foundation Concerning the Reconstruction of the South Eastern Europe*; Editura Politehnica: Timisoara, Romania, 2005; pp. 83–86. ISBN 973.625-204-3.
52. Dearing, J.A. *Environmental Magnetic Susceptibility: Using the Bartington MS2 System*; Chi Publishing: Kenilworth, UK, 1994.
53. Thompson, R.; Oldfield, F. *Environmental Magnetism*; Allen & Unwin: Sydney, Australia, 1986; ISBN 978-94-011-8038-2.
54. Coomarasamy, A.; Walzak, T.L. Effects of Moisture on Surface chemistry of Steel Slags and Steel Slag-Asphalt Paving Mixes. *Transp. Res. Rec.* **1995**.
55. Fällman, A.-M. Leaching of chromium and barium from steel slag in laboratory and field tests—A solubility controlled process? *Waste Manag.* **2000**, *20*, 149–154. [CrossRef]
56. López, F.; López-Delgado, A.; Balcazar, N. Physico-chemical and mineralogical properties of EAF and AOD Slags. *Afinidad* **1996**, *53*, 39–46.
57. Pillay, K.; von Blottnitz, H.; Petersen, J. Ageing of chromium(III)-bearing slag and its relation to the atmospheric oxidation of solid chromium(III)-oxide in the presence of calcium oxide. *Chemosphere* **2003**, *52*, 1771–1779. [CrossRef]
58. Shen, H.; Forssberg, E.; Nordström, U. Physicochemical and mineralogical properties of stainless steel slags oriented to metal recovery. *Resour. Conserv. Recycl.* **2004**, *40*, 245–271. [CrossRef]
59. Suer, P.; Lindqvist, J.-E.; Arm, M.; Frogner-Kockum, P. Reproducing ten years of road ageing—Accelerated carbonation and leaching of EAF steel slag. *Sci. Total Environ.* **2009**, *407*, 5110–5118. [CrossRef]
60. Cabrera-Real, H.; Romero-Serrano, A.; Zeifert, B.; Hernandez-Ramirez, A.; Hallen-Lopez, M.; Cruz-Ramirez, A. Effect of MgO and CaO/SiO_2 on the immobilization of chromium in synthetic slags. *J Mater Cycles Waste Manag.* **2012**, *14*, 317–324. [CrossRef]

61. Huijgen, W.J.J.; Comans, R.N.J. Carbonation of Steel Slag for CO_2 Sequestration: Leaching of Products and Reaction Mechanisms. *Environ. Sci. Technol.* **2006**, *40*, 2790–2796. [CrossRef] [PubMed]
62. Katz, S.A.; Salem, H. The toxicology of chromium with respect to its chemical speciation: A review. *J. Appl. Toxicol.* **1993**, *13*, 217–224. [CrossRef] [PubMed]
63. Jaishankar, M.; Tseten, T.; Anbalagan, N.; Mathew, B.B.; Beeregowda, K.N. Toxicity, mechanism and health effects of some heavy metals. *Interdiscip. Toxicol.* **2014**, *7*, 60–72. [CrossRef] [PubMed]
64. Imtiaz, M.; Rizwan, M.S.; Xiong, S.; Li, H.; Ashraf, M.; Shahzad, S.M.; Shahzad, M.; Rizwan, M.; Tu, S. Vanadium, recent advancements and research prospects: A review. *Environ. Int.* **2015**, *80*, 79–88. [CrossRef] [PubMed]
65. Gustafsson, J.P. Vanadium geochemistry in the biogeosphere—Speciation, solid-solution interactions, and ecotoxicity. *Appl. Geochem.* **2019**, *102*, 1–25. [CrossRef]
66. Gupta, U.C. Symptoms of Molybdenum Deficiency and Toxicity in Crops. In *Molybdenum in Agriculture*; Gupta, U.C., Ed.; Cambridge University Press: Cambridge, UK, 1997; pp. 160–170. ISBN 978-0-521-57121-0.
67. Kubota, J.; Lazar, V.A.; Simonson, G.H.; Hill, W.W. The Relationship of Soils to Molybdenum Toxicity in Grazing Animals in Oregon. *Soil Sci. Soc. Am. J.* **1967**, *31*, 667–671. [CrossRef]
68. Matern, K.; Rennert, T.; Mansfeldt, T. Molybdate adsorption from steel slag eluates by subsoils. *Chemosphere* **2013**, *93*, 2108–2115. [CrossRef]
69. Lee, Y.; Nassaralla, C.L. Formation of hexavalent chromium by reaction between slag and magnesite-chrome refractory. *Met. Mater. Trans B* **1998**, *29*, 405–410. [CrossRef]
70. Ziemniak, S.E.; Castelli, R.A. Immiscibility in the FeS_3O_4–$FeCr_2O_4$ spinel binary. *J. Phys. Chem. Solids* **2003**, *64*, 2081–2091. [CrossRef]